Model Predictive Control of Load Commutated Inverter-fed Synchronous Machines

Thomas Besselmann, Stefan Almér and Hans Joachim Ferreau

Abstract—The paper at hand considers torque regulation of a variable speed synchronous machine fed by a line commutated rectifier and a load commutated inverter. The proposed control approach is model predictive control where both the rectifier and inverter firing angles are considered as control inputs. Conventional controllers assign different tasks to the rectifier and inverter firing angle. In contrast, the model predictive controller coordinates the firing angles and this improves the dynamic performance and disturbance rejection. In particular, the proposed controller handles line side under voltage conditions better than a conventional PI controller. The nonlinear model predictive torque controller has been implemented on an embedded system and applied in an experimental test bed. The experiments confirm that the controller is able to successfully ride through line side under voltage conditions.

Index Terms—AC motor drives, Synchronous machines, Predictive control, Availability.

I. INTRODUCTION

THE SUBJECT MATTER of this paper is torque control of a variable speed synchronous machine connected to the grid via a line commutated rectifier and a load commutated inverter (LCI) [1]–[4]. This type of variable speed solution is often the preferred choice in high power applications, ranging from a few megawatts to over a hundred megawatts, [5], [6].

The work is motivated mainly by electrically-driven gas compression plants which are often situated in remote locations and operate under weak grid conditions. Weather phenomena occasionally produce sudden sags of the grid voltage, which can cause the drive to trip, interrupting or even aborting the gas compression process. The goal of this work is to design a more agile torque controller to increase the system robustness to external disturbances. In particular, we want to improve the ability to reliably ride through power loss situations due to grid faults and deliver torque during partial loss of grid voltage, [7].

The model predictive control (MPC) approach proposed in this work minimizes the deviation of the torque from the reference while respecting constraints on the state and control inputs. The MPC formulation considers both the rectifier and inverter firing angles as control inputs and stabilizes the DC link current and rotor flux while tracking the torque reference.

The authors are with ABB Corporate Research, Segelhofstrasse 1K, 5405 Baden-Dättwil, Switzerland (e-mail: thomas.besselmann@ch.abb.com; stefan.almer@ch.abb.com; joachim.ferreau@ch.abb.com).

Conventional PI-based control approaches typically assign different tasks to the two control inputs, *i.e.*, the rectifier and inverter firing angles. The inverter angle is used to regulate the power factor of the machine and is typically chosen from a look-up table by feed forward control. The rectifier angle is used to control the DC link current. The fact that the MPC controls the rectifier and inverter angles without pre-assigning tasks to them implies a potential for better disturbance rejection. In particular, in the case of a disturbances to the line voltage the PI would only adjust the rectifier angle while the MPC would adjust both firing angles. The MPC approach is thus expected to handle larger disturbances to the line voltage.

In recent years there has been considerable interest in MPC for control of converters and electric machines. However, the focus of most research has been on voltage source converter topologies. In the present paper we consider a synchronous machine fed by *current source* converters. To the best of our knowledge, MPC has not been applied to LCI-fed synchronous machines prior to the presented line of research. Recent work on control of LCIs, employing other methods than MPC, can be found in [8], [9].

The literature on MPC of power electronics is to a large extent focused on so-called finite control set model predictive control (FCS-MPC), see *e.g.*, [10]–[12]. In FCS-MPC, the converter switches are controlled directly. The state of the switches (on/off) is represented by binary variables and the control problem is thus a pure integer optimization problem. This problem is usually solved by enumerating all possible binary combinations over the prediction horizon. The FCS-MPC approach has certain drawbacks, including very short prediction horizon, chattering and unpredictable and time varying switching frequency.

The drawbacks of FCS-MPC are mitigated by considering the use of a modulator which maps a continuous control variable, such as a duty-cycle or a firing angle, to switching action, see *e.g.*, [13]–[18]. The control approach outlined in the present paper belongs to the later class of methods which considers a continuous control variable.

Implementing the model predictive controller requires to solve a constrained nonlinear, nonconvex optimization problem in real-time. This is a challenging task as our application requires a sampling time of one millisecond and the embedded computing power is limited. Solving nonlinear MPC problems in such a situation requires both a careful problem formulation and highly efficient, state-of-the-art optimization algorithms. In this paper, we follow the promising approach of auto-generating customized nonlinear MPC algorithms that are tailored to the problem at hand based on a symbolic problem formulation as proposed in [19].
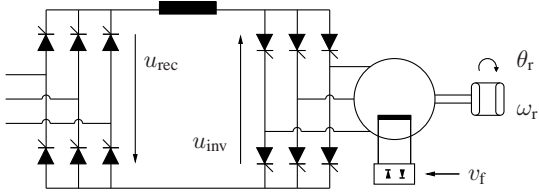
Fig. 1: Variable speed drive system comprised of line commutated rectifier, inductive DC link, load commutated inverter and synchronous machine.

A preliminary version of this work was presented in the conference paper [20]. The paper at hand extends this line of research (a) in its theoretical content by providing a more detailed description of the dynamic model of the system at hand and of the proposed control system; and (b) in its practical content by presenting an experimental validation of the proposed control solution, which required the implementation of a nonlinear MPC algorithm on an embedded platform.

The paper is organized as follows. In Section II we describe the synchronous machine and the load-commutated inverter. A mathematical model of this system is presented in Sections III and IV. The developed control solution including the MPC torque controller and the state estimation is described in Section V. Section VI contains experimental results. Finally, conclusions are drawn in Section VII.

The subindices 'd' and 'q' represent the components in the rotor-aligned dq-reference frame, whereas the subindices 'x' and 'y' represent components of the stator-aligned xy-reference frame, [21]. Estimated variables are marked with a hat (*i.e.* $\hat{\cdot}$). Note that all quantities in this paper are normalized quantities.

II. CURRENT SOURCE CONVERTERS AND SYNCHRONOUS MACHINE

The paper considers a variable speed drive system composed of a line commutated rectifier, inductive DC link, load commutated inverter and a synchronous machine, see Fig. 1. In the considered configuration the rectifier and inverter consist of six pulse thyristor bridges. However, the proposed control scheme can easily be adapted to other configurations, such as twelve pulse bridges and poly-phase synchronous machines as was considered in [20]. This type of drive systems is suitable for high power applications ranging from a few megawatts to over a hundred megawatts. Such applications include high speed compressors and rolling mills.

The control inputs (signals to be manipulated by the controller) are the firing angle α of the line side rectifier and firing angle β of the machine side inverter. Furthermore, the excitation flux ψ_f is controlled by an excitation voltage v_f. The variable to be controlled is the air gap torque produced by the synchronous machine.

III. THYRISTOR BRIDGE MODEL

The present section describes how the DC side voltage and AC side current of the thyristor bridges are modeled. For the sake of simplicity we assume instantaneous switchings and
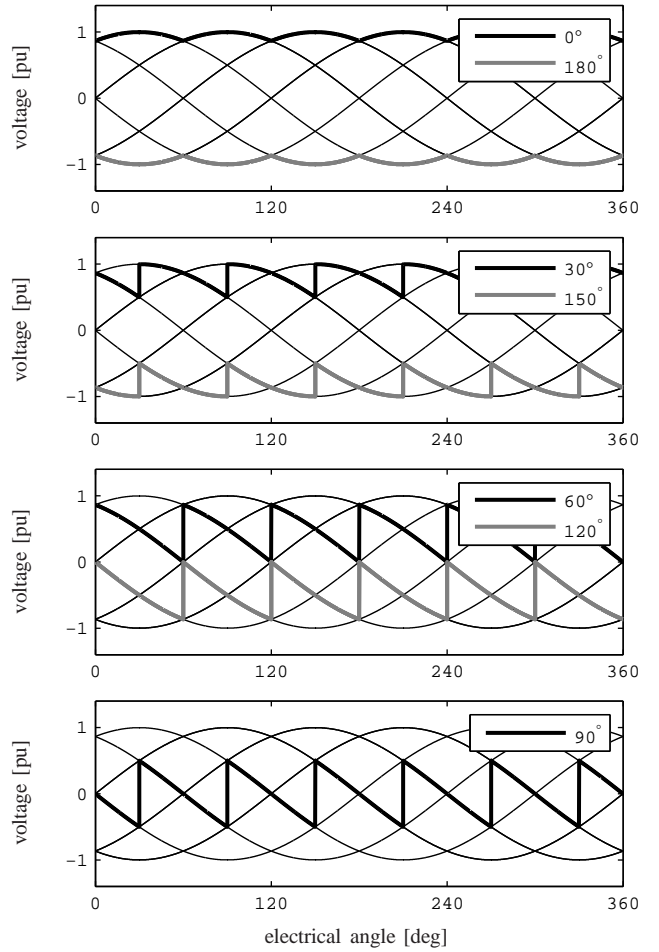

Fig. 2: AC and DC side voltages of a six-pulse thyristor bridge over one period of the AC side voltage. The thin lines show the line-to-line voltages on the AC side. The thick lines show the switched voltage of the DC side for different values of the firing angle.

neglect phenomena such as commutation overlap, thyristor recharge time, forced commutation at low speeds, asymmetric grid conditions or intermittent operation at low DC current.

A. Thyristor Bridge DC Voltage

The DC side voltage of the thyristor bridges in Fig. 1 is a switched waveform which is constructed by switching between the AC side line-to-line voltages. The principle is illustrated in Fig. 2 where the sinusoids represent the line-to-line voltages on the AC side and where the thick lines illustrate the DC side voltage for a few different values of the firing angle which ranges from 0 to 180 degree. The firing angle determines the time instant of the switch from one line-to-line voltage to another and this determines the average value of the DC side voltage. For a firing angle of 0 degree the thyristor bridge operates identical to a diode bridge, where the instant value of the line-to-line voltages determines which diodes are conducting. Larger firing angles represent the time delay of the thyristor bridge switchings compared to the switchings of a diode bridge.
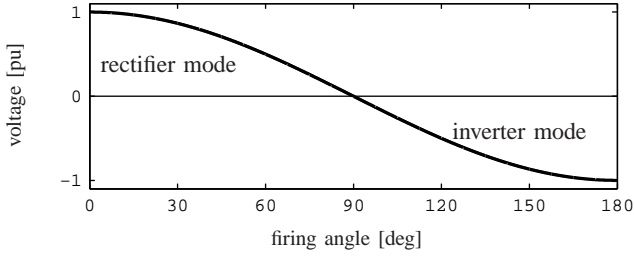
Fig. 3: DC side approximation: Approximate relation between AC and DC voltages of a thyristor bridge. The DC side voltage is approximated by a cosine of the firing angle.
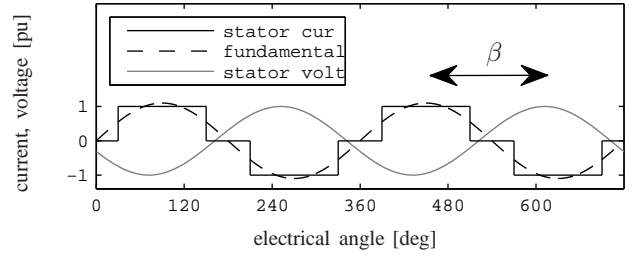

Fig. 4: AC side approximation: Stator current and its fundamental, and stator voltage of the synchronous machine. The power factor is determined by the angle β between current and voltage.

For the purpose of control, we describe the average value of the switched DC side voltage as a function of the firing angle. The thyristor bridge DC voltage is approximated by a cosine of the firing angle as illustrated in Fig. 3. The approximation is intuitively clear considering the waveforms in Fig. 2. A derivation can be found in [22]. The thyristor bridge can operate as rectifier and as inverter, depending on the choice of firing angle. Neglecting the switching we have

$$u_{\text{rec}} \approx k_1 u_{\text{l}} \cos(\alpha), \quad u_{\text{inv}} \approx k_1 \|\mathbf{U}_{\text{s}}\| \cos(\beta), \tag{1}$$

where u_{rec} and u_{inv} are the DC side voltages of the line side and the machine side thyristor bridges, respectively, k_1 is a constant, u_{l} is the amplitude of the line voltage and $\|\mathbf{U}_{\text{s}}\|$ is the amplitude of the stator voltage, [23].

We note that the thyristors can be turned on at any time, but they can only be turned off by reducing the current running through them to zero. Thus, the off-switching of the thyristors is state dependent. This is neglected in the control model.

B. Thyristor Bridge AC Current

The AC side inverter current is illustrated in Fig. 4. The ideal waveform (neglecting commutation time [24]) is piecewise constant. For the purpose of control, the AC current is approximated by its fundamental component, which is illustrated by the dashed line in Fig. 4.

The modulator of the inverter, which takes the angle β and controls the switching, places the stator current at an angle β to the stator voltage. and thus controls the power factor of the machine. The dq reference frame is rotor oriented and the angle δ of the stator voltage in the dq frame therefore appears in the dynamic equations below. The angular relationships of the machine state is illustrated in Fig. 5. Note that the direction of positive current is different for the synchronous machine and the thyristor bridge model, such that in Fig. 5, β is the angle between the stator voltage and the negative stator current.

Approximating the stator current by its fundamental component and transforming it into the dq-frame yields

$$\mathbf{I}_{\text{s}} \approx k_2 i_{\text{dc}} \begin{bmatrix} \cos(-\beta + \delta) \\ \sin(-\beta + \delta) \end{bmatrix}, \tag{2}$$

where k_2 is a constant and where δ denotes the orientation of the stator voltage in the dq-frame.
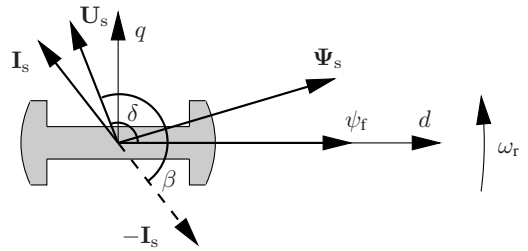

Fig. 5: Machine state in rotor oriented reference frame.

IV. PREDICTION MODEL

The MPC torque controller is based on the dynamic model of the DC link and synchronous machine developed below.

A. Control Input, State and Parameters

In deriving a dynamic model of the system suitable for torque control, we first decide which system quantities to model as states and which to consider as parameters. Certain quantities are assumed to vary sufficiently slow to be approximated as constant when regulating the torque and are considered as parameters. These quantities are the line voltage amplitude u_{l}, the mechanical rotor angular frequency ω_{r} the angle δ of the stator voltage w.r.t. the rotor and the rotor excitation flux ψ_{f}. We note that the rotor excitation flux ψ_{f} is controlled by a separate PI controller which adjusts the excitation voltage to control ψ_{f}. The decision to treat ψ_{f} as a parameter is motivated by the fact that ψ_{f} is controlled in closed loop. The design of the excitation control is not discussed in this paper The control variable (excitation voltage) v_{f} is therefore not considered in the sequel.

The state of the system consists of the DC link current i_{dc} and the machine damper winding flux linkages ψ_{rd} and ψ_{rq}. The state is described in the rotor oriented rotating frame, see Fig. 5. The control input is the rectifier firing angle α and inverter firing angle β.

B. State Dynamics

Let $\mathbf{\Psi}_{\text{r}}$ and $\mathbf{I}_{\text{r}}$ be the vector of damper winding flux linkages and currents respectively. The damper flux linkage satisfies [25]

$$\frac{d}{dt}\mathbf{\Psi}_{\text{r}} = \mathbf{R}_{\text{r}}\mathbf{I}_{\text{r}}, \quad \mathbf{R}_{\text{r}} := \omega_{\text{N}} \begin{bmatrix} -r_{\text{d}} & 0 \\ 0 & -r_{\text{q}} \end{bmatrix}, \tag{3}$$

where r_d and r_q are the damper winding resistances and where ω_N is the nominal rotor frequency. We note that the equations are in per unit, so that the units of the left and right hand side above match. A reformulation of the current-flux relations of the synchronous machine is provided in the appendix. Using expression (29) in the appendix for the vector of damper winding currents, the damper flux linkage dynamics can be written as

$$\frac{d}{dt}\mathbf{\Psi}_r = \mathbf{A}\mathbf{\Psi}_r + \mathbf{B}\mathbf{I}_s + \mathbf{F}\psi_f, \tag{4}$$

where

$$\mathbf{A} := \mathbf{R}_r\mathbf{M}_2, \quad \mathbf{B} := \mathbf{R}_r\mathbf{M}_1, \quad \mathbf{F} := \mathbf{R}_r\mathbf{M}_3, \tag{5}$$

and where $\mathbf{M}_1$, $\mathbf{M}_2$, $\mathbf{M}_3$ are defined in (29).

Inserting approximation (2) in (4), we get the following differential equation for the damper winding flux linkage

$$\frac{d}{dt}\mathbf{\Psi}_r = \mathbf{A}\mathbf{\Psi}_r + k_2\mathbf{B}i_{dc}\begin{bmatrix}\cos(-\beta+\delta)\\\sin(-\beta+\delta)\end{bmatrix} + \mathbf{F}\psi_f. \tag{6}$$

We note that the dynamics are nonlinear and that the nonlinear term links the damper winding flux linkage and the DC link current.

The DC link current dynamics are described by

$$\frac{d}{dt}i_{dc} = \frac{1}{L_{dc}}\Big(-r_{dc}i_{dc} + u_{rec} + u_{inv}\Big), \tag{7}$$

where L_{dc}, r_{dc} are the inductance and parasitic resistance of the DC link inductor and where u_{rec} and u_{inv} are the DC voltage of the rectifier and inverter bridges, respectively.

We adopt the average model (1) described in Section III above to describe the relation between the AC and DC side voltages of the rectifier and inverter. The line voltage amplitude u_l is a parameter in the MPC problem formulation. The stator voltage amplitude $\|\mathbf{U}_s\|$ of the machine is a (nonlinear) function of the system state. In order to formulate a state space model for the damper winding flux linkage and DC link dynamics we need to make this relationship explicit, which is done next.

Let $\mathbf{U}_s$ and $\mathbf{\Psi}_s$ be the stator voltage and stator flux, respectively. Stated in the dq-reference frame, the stator voltage satisfies the voltage equation

$$\mathbf{U}_s = \mathbf{R}_s\mathbf{I}_s + \frac{d}{dt}\mathbf{\Psi}_s + \omega_r\mathbf{S}\mathbf{\Psi}_s, \tag{8}$$

where

$$\mathbf{R}_s = \begin{bmatrix}r_s & 0\\0 & r_s\end{bmatrix}, \quad \mathbf{S} = \begin{bmatrix}0 & -1\\1 & 0\end{bmatrix}, \tag{9}$$

where r_s is the stator resistance. The flux satisfies the relation

$$\mathbf{\Psi}_s = \mathbf{M}_4\mathbf{I}_s + \mathbf{M}_5\mathbf{\Psi}_r + \mathbf{M}_6\psi_f, \tag{10}$$

see (30) in the appendix for an outline on how to derive the matrices $\mathbf{M}_4$, $\mathbf{M}_5$, $\mathbf{M}_6$. To obtain an expression for $\mathbf{U}_s$ as a function of the state we substitute expression (10) into (8) while applying the approximations

$$\frac{d}{dt}\mathbf{I}_s \approx 0, \tag{11a}$$

$$\frac{d}{dt}\psi_f \approx 0. \tag{11b}$$

Approximation (11a) is a standard assumption in control of current source fed synchronous machines [24]. In this paper, the approximation is made to obtain an explicit expression for $\mathbf{U}_s$ as a function of the state. Note that only the effect of the stator current derivative on the stator voltage is neglected, whereas the derivative of the DC current (which is related to the derivative of the stator current) enters the prediction model by means of equation (7). Approximation (11b) is motivated by the fact that the excitation flux is controlled by a separate controller as discussed in Section IV-A. Moreover, the excitation flux varies considerably slower than the other state variables.

The approximation yields

$$\mathbf{U}_s \approx \mathbf{R}_s\mathbf{I}_s + \mathbf{M}_5\frac{d}{dt}\mathbf{\Psi}_r + \omega_r\mathbf{S}(\mathbf{M}_4\mathbf{I}_s + \mathbf{M}_5\mathbf{\Psi}_r + \mathbf{M}_6\psi_f). \tag{12}$$

Inserting expression (4) into the expression above yields

$$\mathbf{U}_s \approx \mathbf{\Gamma}_1(\omega_r)\mathbf{I}_s + \mathbf{\Gamma}_2(\omega_r)\mathbf{\Psi}_r + \mathbf{\Gamma}_3(\omega_r)\psi_f, \tag{13}$$

where

$$\begin{aligned}\mathbf{\Gamma}_1(\omega_r) &:= \mathbf{R}_s + \mathbf{M}_5\mathbf{B} + \omega_r\mathbf{S}\mathbf{M}_4,\\\mathbf{\Gamma}_2(\omega_r) &:= \mathbf{M}_5\mathbf{A} + \omega_r\mathbf{S}\mathbf{M}_5,\\\mathbf{\Gamma}_3(\omega_r) &:= \mathbf{M}_5\mathbf{F} + \omega_r\mathbf{S}\mathbf{M}_6.\end{aligned} \tag{14}$$

Applying the averaged approximation (2) we finally obtain the following (approximate) expression for $\mathbf{U}_s$

$$\mathbf{U}_s \approx k_2\mathbf{\Gamma}_1(\omega_r)i_{dc}\begin{bmatrix}\cos(-\beta+\delta)\\\sin(-\beta+\delta)\end{bmatrix} + \mathbf{\Gamma}_2(\omega_r)\mathbf{\Psi}_r + \mathbf{\Gamma}_3(\omega_r)\psi_f. \tag{15}$$

C. Torque Expression

The MPC problem formulation penalizes the deviation of the torque from a given reference and we therefore need an expression for the torque. The torque is given by

$$t_e = \psi_{sd}i_{sq} - \psi_{sq}i_{sd}, \tag{16}$$

where ψ_{sd}, ψ_{sq}, i_{sd}, i_{sq} are the stator fluxes and currents. Using the flux linkage equations (29)-(30) and the averaged approximation (2) of how the stator current depends on the inverter firing angle, the torque can be expressed as a nonlinear function of the system state

$$\begin{aligned}t_e &\approx (k_2 i_{dc})^2 \begin{bmatrix}\cos(-\beta+\delta)\\\sin(-\beta+\delta)\end{bmatrix}' \mathbf{S}\mathbf{M}_4 \begin{bmatrix}\cos(-\beta+\delta)\\\sin(-\beta+\delta)\end{bmatrix}\\ &+ k_2 i_{dc}\begin{bmatrix}\cos(-\beta+\delta)\\\sin(-\beta+\delta)\end{bmatrix}\mathbf{S}\left(\mathbf{M}_5\mathbf{\Psi}_r + \mathbf{M}_6\psi_f\right).\end{aligned} \tag{17}$$

D. Model Summary

The dynamic model of the synchronous machine, converters and DC link used in the MPC problem formulation is
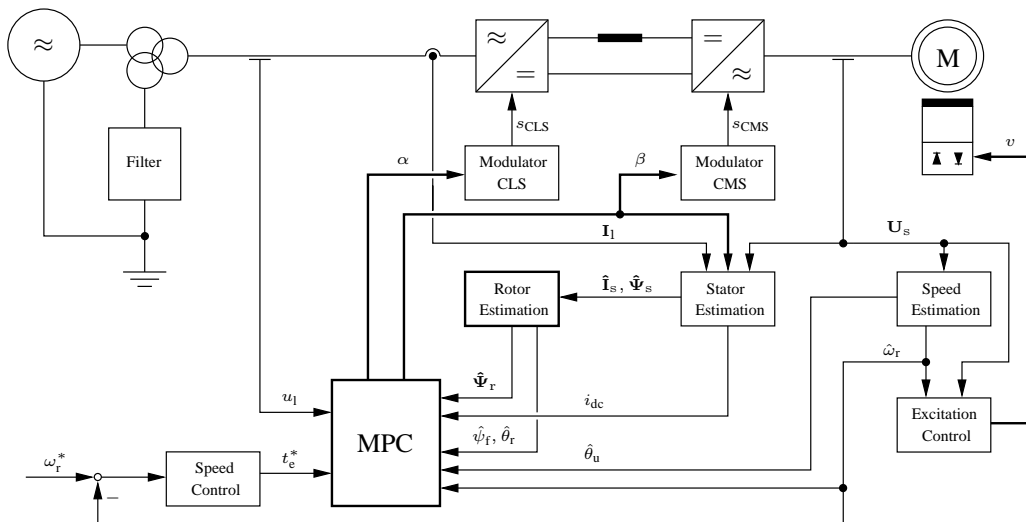
Fig. 6: Overview of the proposed control solution for load commutated inverter-fed synchronous machines.

$$\frac{d}{dt}\boldsymbol{\Psi}_{\mathrm{r}} = \mathbf{A}\boldsymbol{\Psi}_{\mathrm{r}} + k_2\mathbf{B}i_{\mathrm{dc}}\begin{bmatrix}\cos(-\beta+\delta)\\\sin(-\beta+\delta)\end{bmatrix} + \mathbf{F}\psi_{\mathrm{f}}, \tag{18a}$$

$$\frac{d}{dt}i_{\mathrm{dc}} = \frac{1}{L_{\mathrm{dc}}}\left(-r_{\mathrm{dc}}i_{\mathrm{dc}} + u_{\mathrm{l}}k_1\cos(\alpha) + \|\mathbf{U}_{\mathrm{s}}\|k_1\cos(\beta)\right), \tag{18b}$$

$$\mathbf{U}_{\mathrm{s}} = \boldsymbol{\Gamma}_1(\omega_{\mathrm{r}})i_{\mathrm{dc}}\begin{bmatrix}\cos(-\beta+\delta)\\\sin(-\beta+\delta)\end{bmatrix} + \boldsymbol{\Gamma}_2(\omega_{\mathrm{r}})\boldsymbol{\Psi}_{\mathrm{r}} + \boldsymbol{\Gamma}_3(\omega_{\mathrm{r}})\psi_{\mathrm{f}}, \tag{18c}$$

$$t_{\mathrm{e}} = (k_2i_{\mathrm{dc}})^2\begin{bmatrix}\cos(-\beta+\delta)\\\sin(-\beta+\delta)\end{bmatrix}'\mathbf{SM}_4\begin{bmatrix}\cos(-\beta+\delta)\\\sin(-\beta+\delta)\end{bmatrix}$$
$$+ k_2i_{\mathrm{dc}}\begin{bmatrix}\cos(-\beta+\delta)\\\sin(-\beta+\delta)\end{bmatrix}'\mathbf{S}\left(\mathbf{M}_5\boldsymbol{\Psi}_{\mathrm{r}} + \mathbf{M}_6\psi_{\mathrm{f}}\right), \tag{18d}$$

where the matrices are defined in (5) and (14).

V. PROPOSED CONTROL SOLUTION

A simplified block diagram of the proposed control solution is shown in Fig. 6. Parts of the solution are state of the art and have been discussed in previous work, see *e.g.* [22], [26]. For brevity we thus focus on the innovative part of the control system, being the model predictive torque controller and an extended Kalman filter (EKF) for rotor state estimation.

A. Model Predictive Torque Controller

At each sampling time, the model predictive controller takes an estimate of the system state as initial condition and minimizes a finite time horizon cost integral subject to the dynamic constraints of the system and constraints on the state and input. The cost criterion is

$$J := \int_{kT_{\mathrm{s}}}^{kT_{\mathrm{s}}+T_{\mathrm{p}}} (t_{\mathrm{e}} - t_{\mathrm{e}}^*)^2\,dT, \tag{19}$$

where T_{s} is the sampling period, T_{p} is the prediction horizon length and t_{e}^* is the torque reference. We note that the cost criterion can be augmented to penalize state variables and

control input without any fundamental changes to how the optimization problem is solved, which is described below.

Model predictive control allows for the intuitive observance of constraints on inputs, states and outputs. In the application at hand we limit the eligible firing angles and request an upper bound on the DC current,

$$\alpha_{\min} \leq \alpha \leq \alpha_{\max}, \quad \beta_{\min} \leq \beta \leq \beta_{\max}, \quad i_{\mathrm{dc}} \leq i_{\mathrm{dc,max}}, \tag{20}$$

for some application-dependent bounds. The optimal control problem can thus be stated as

$$\min_{\alpha,\beta} \ (19) \quad \text{s.t.} \quad (18),(20). \tag{21}$$

In order to solve the optimal control problem (21), it first needs to be discretized in time to yield a finite-dimensional numerical optimization problem. If the dynamic model were linear, one would only need to perform this problem discretization once before the actual runtime of the controller. In that case, the only computational effort to be performed on-line would be to solve a convex quadratic programming (QP) problem. Recent years have seen a rapid development of on-line QP solvers that are able to solve such kind of linear MPC problems in the milli- or even microsecond range on embedded hardware, see *e.g.* [16], [27], [28].

However, since our system model is nonlinear, optimal control problem (21) does not result in a QP problem, but in a general nonconvex nonlinear programming (NLP) problem. This has two main consequences: first, we are forced to discretize problem (21) on-line at each sampling instant; second, we need to employ a method for solving NLP problems (see e.g. [29] for an overview). Among the methods for solving NLP problems are sequential quadratic programming (SQP) methods. One paticular SQP method tailored to solving nonlinear MPC problems is the so-called real-time iteration (RTI) scheme with Gauss-Newton approximation of the second-order derivatives [30]. At each sampling instant, the RTI scheme not only discretizes problem (21) in time but also computes first-order derivatives of the state trajectory with respect to the initial state value and the control moves along
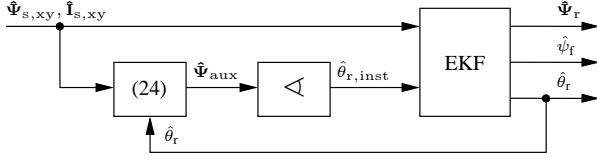
Fig. 7: Block diagram of the rotor estimation.

the horizon (also called sensitivities). In doing so, one obtains a discrete-time linearization of the optimal control problem, which corresponds to a convex QP problem. For solving this QP problem efficiently, we choose to eliminate all state variables from the QP formulation to arrive at a smaller-scale, dense QP problem, which is then solved by the embedded variant of the on-line QP solver qpOASES [31].

In order to obtain a highly efficient implementation of the nonlinear MPC algorithm, namely the SQP-based RTI scheme as sketched above, we make use of the code generation functionality of the ACADO Toolkit [19]. This software takes a symbolic formulation of the control problem and allows the user to automatically generate customized nonlinear MPC algorithms that are tailored to the specific problem structure. The resulting C code is self-contained, highly optimized and able to run on embedded computing hardware. In our case, the MPC controller runs on ABB's controller AC 800PEC, which is based on a 32-bit Power PC processor with a clock speed of up to 600 MHz and also includes an FPGA and a 64-bit IEEE floating point unit. On this platform, the controller has been shown to execute in less than 1 millisecond.

B. State Estimation

The MPC assumes that measurements or estimates of the entire system state $\mathbf{x} := \begin{bmatrix} \psi_{rd}, & \psi_{rq}, & i_{dc} \end{bmatrix}'$ and of the parameter $\mathbf{p} := \begin{bmatrix} u_1, & \psi_f, & \omega_r, & \delta \end{bmatrix}'$ are fed to the controller at each sampling time. In the present paper we do *not* assume that these quantities are measured. Instead, they are estimated by an observer. The input to the observer are quantities which are typically measured in an industrial application. These are the grid voltage $\mathbf{U}_1$, the grid current $\mathbf{I}_1$ and the stator voltage $\mathbf{U}_s$, see Fig. 6. While the DC current i_{dc} and the line side voltage magnitude can be deduced directly from the line side current $\mathbf{I}_1$ and voltage $\mathbf{U}_1$, respectively, other quantities such as the damper winding flux linkage $\mathbf{\Psi}_r$ require a more sophisticated approach. This section shows how the estimates are obtained. See e.g. [1], [22], [26] and the reference therein for more details on state estimation in synchronous machines.

Figure 6 depicts the structure of the state estimation which comprises three parts; a speed estimation, a stator flux estimation and rotor flux estimation by means of an extended Kalman filter [32]. The reason for this separation is that the speed and stator flux estimation run at a higher sampling rate in order to increase the estimation accuracy, while the EKF runs with a lower sampling rate to keep the computational costs at bay.

1) Speed estimation: The speed estimation provides estimates of the rotor speed $\hat{\omega}_r$ and the orientation $\hat{\theta}_u$ of the stator voltage. This information can be derived from the stator voltage $\mathbf{U}_s$, *e.g.* by means of a phase lock loop (PLL).

2) Stator estimation: The purpose of the stator estimator is the deduction of stator current and stator flux. Since no measurements of the stator current are available, the stator estimator deduces the DC link current i_{dc} from the line side current $\mathbf{I}_1$; and the stator winding current $\mathbf{I}_{s,xy} = [i_{sx}, i_{sy}]'$ from the DC link current i_{dc} and the switching positions s_{CMS} of the machine side thyristor bridge. The current in the DC link flows through the stator as well, and the switching positions indicate which phases are connected to the DC link. Thus an estimate of the stator current can be deduced.

Taking the stator winding current and voltage in xy-coordinates and using the so-called voltage model

$$\mathbf{U}_s = \mathbf{R}_s\mathbf{I}_s + \frac{d}{dt}\mathbf{\Psi}_s, \tag{22}$$

an estimate of the stator flux $\hat{\mathbf{\Psi}}_{s,xy} = [\hat{\psi}_{sx}, \hat{\psi}_{sy}]'$ can be obtained by integration.

3) Rotor estimation: Subsequently the stator current and the estimate of the stator flux are the inputs to the rotor estimator, which provides estimates of the rotor position and the rotor fluxes, *i.e.* the excitation and damper winding flux linkages. A block diagram of the rotor estimator is depicted in Figure 7, [1]. The rotor estimator is comprised of an estimate of the rotor angle and an extended Kalman filter. Supplying the EKF with an estimate of the rotor angle has improved the estimation accuracy.

This rotor angle estimate can be derived as follows. By means of the transformation matrix

$$\mathbf{P}(\theta_r) := \begin{bmatrix} \cos(\theta_r) & \sin(\theta_r) \\ -\sin(\theta_r) & \cos(\theta_r) \end{bmatrix}, \tag{23}$$

which links the dq and the xy reference frame, the upper part of the flux-linkage equations (27) can be reformulated as

$$\mathbf{P}\begin{bmatrix} \psi_{sx} \\ \psi_{sy} \end{bmatrix} - \begin{bmatrix} L_{sd} & 0 \\ 0 & L_{sq} \end{bmatrix}\mathbf{P}\begin{bmatrix} i_{sx} \\ i_{sy} \end{bmatrix} = \underbrace{\begin{bmatrix} L_{md} & 0 \\ 0 & L_{mq} \end{bmatrix}\begin{bmatrix} i_{rd} + i_f \\ i_{rq} \end{bmatrix}}_{\mathbf{\Psi}_{aux}}. \tag{24}$$

See the appendix for more details on the flux-linkage equation. The auxiliary flux variable $\hat{\mathbf{\Psi}}_{aux}$ is calculated at each time instance from the stator quantities using (24). It follows from Eq. (3) that the current i_{rq} in the quadrature damper windings must vanish on average if the quadrature damper winding linkage is not to grow unboundedly. Thus the angle of $\hat{\mathbf{\Psi}}_{aux}$ constitutes an instantaneous estimate of the rotor angle, $\hat{\theta}_{r,inst}$. This angle is fed together with the stator quantities to an extended Kalman filter.

The EKF itself is based on a dynamic model of the synchronous machine, similar to the one described in Section IV:

Fig. 8: Motor configuration at the test bed with the synchronous machine and a DC machine used as load.

$$\frac{d}{dt}\mathbf{\Psi}_{\mathrm{r}} = \mathbf{A}\mathbf{\Psi}_{\mathrm{r}} + \mathbf{B}\mathbf{I}_{\mathrm{s}} + \mathbf{F}\psi_{\mathrm{f}}, \tag{25a}$$

$$\frac{d}{dt}\psi_{\mathrm{f}} = -\omega_N r_{\mathrm{f}}i_{\mathrm{f}} + \omega_N u_{\mathrm{f}}, \tag{25b}$$

$$\frac{d}{dt}u_{\mathrm{f}} = 0, \tag{25c}$$

$$\frac{d}{dt}\theta_r = -\omega_N\omega_{\mathrm{r}}, \tag{25d}$$

$$\frac{d}{dt}\omega_{\mathrm{r}} = 0, \tag{25e}$$

with

$$\begin{bmatrix}\psi_{\mathrm{sd}}, & \psi_{\mathrm{sq}}\end{bmatrix}' = \mathbf{P}(\theta_r)\begin{bmatrix}\psi_{\mathrm{sx}}, & \psi_{\mathrm{sy}}\end{bmatrix}', \tag{25f}$$

$$\begin{bmatrix}i_{\mathrm{sd}}, & i_{\mathrm{rd}}, & i_{\mathrm{f}}\end{bmatrix}' = \mathbf{L}_{\mathrm{d}}^{-1}\begin{bmatrix}\psi_{\mathrm{sd}}, & \psi_{\mathrm{rd}}, & \psi_{\mathrm{f}}\end{bmatrix}', \tag{25g}$$

$$\begin{bmatrix}i_{\mathrm{sq}}, & i_{\mathrm{rq}}\end{bmatrix}' = \mathbf{L}_{\mathrm{q}}^{-1}\begin{bmatrix}\psi_{\mathrm{sq}}, & \psi_{\mathrm{rq}}\end{bmatrix}', \tag{25h}$$

$$\begin{bmatrix}i_{\mathrm{sx}}, & i_{\mathrm{sy}}\end{bmatrix}' = \mathbf{P}(\theta_r)^{-1}\begin{bmatrix}i_{\mathrm{sd}}, & i_{\mathrm{sq}}\end{bmatrix}', \tag{25i}$$

where $\mathbf{L}_{\mathrm{d}}$, $\mathbf{L}_{\mathrm{q}}$ are defined in the appendix. While the estimated stator flux serves as input, the stator current and the instantaneous rotor angle estimate serve as outputs to the model. From the states of the estimation model (25), the estimated rotor quantities $\begin{bmatrix}\hat{\mathbf{\Psi}}_{\mathrm{r}}, & \hat{\psi}_{\mathrm{f}}, & \hat{\theta}_{\mathrm{r}}\end{bmatrix}'$, are supplied to the MPC. The relative position of the stator voltage w.r.t. the rotor can be computed as $\hat{\delta} = \hat{\theta}_{\mathrm{u}} - \hat{\theta}_{\mathrm{r}}$.

VI. EXPERIMENTAL EVALUATION

The MPC torque controller was tested on a test bed composed of a low-voltage LCI powering a 11.6 kW synchronous machine. The synchronous machine is depicted together with a DC load motor in Figure 8. The design data of the test bed can be found in Table I.

The controller was implemented on ABB's AC 800PEC, described in Section V-A above. The sampling period T_{s} was 1 ms. The cost function (19) was extended to

$$J := \int_{kT_{\mathrm{s}}}^{kT_{\mathrm{s}}+T_{\mathrm{p}}} Q(t_{\mathrm{e}} - t_{\mathrm{e}}^*)^2 + R(\beta - \beta^*)^2 \, dT, \tag{26}$$

with $Q = 1, R = 0.1, T_p = 10\,\mathrm{ms}$. We note that adding the penalty on the firing angle β means that the controller will,

if possible, choose β to equal the reference value, and select any feasible α which is needed to obtain the requested torque. Since Q and R are scalar, it follows that there is only one degree of freedom in the tuning parameters, namely the ratio between Q and R. This ratio is chosen based on two criteria which are evaluated in simulation: Firstly, we consider the step response to changes in the torque reference. Secondly, we consider the variation of the control input at steady state operation. The ratio between Q and R is chosen to give a good trade-off between a fast transient response and a steady state with small variability in the firing angles. The prediction horizon T_{p} is chosen to be an order of magnitude larger than the sampling time.

The upper bound on the DC current was set to $i_{\mathrm{dc,max}} = 1\,\mathrm{pu}$, while the firing angles were limited to the range $0 \leq \alpha \leq 145\,\mathrm{deg}$, $35 \leq \beta \leq 145\,\mathrm{deg}$.

A. Torque Step Test

Firstly the reaction of the proposed control solution to changes in the reference torque was tested. In this scenario the speed controller provides a torque reference for the synchronous machine to rotate with 0.5 pu speed in steady state. At time zero the torque reference of the speed controller is overwritten by a torque reference of 1 pu for 40 ms. Then the torque reference is set to -1 pu for another 40 ms. Finally the speed controller resumes control again.

Figure 9 shows the reactions of the MPC scheme and of a state-of-the-art PI controller. For the positive torque step, the MPC achieves a rise time of under 10 ms, compared to more than 20 ms for the PI controller. The change from accelerating to breaking shows an even bigger difference in behaviour. The PI controller waits for 20 ms before it reacts at all. Then it discharges the DC link before starting to break. The total delay is nearly 35 ms, such that it barely breaks at all within the 40 ms window. In contrast the MPC changes smoothly from accelerating to breaking, without discharging the DC link.

B. Circuit Breaker Test

In order to test the resilience of the MPC scheme during temporary voltage outages, the main circuit breaker of the LCI was opened briefly under various operating conditions as summarized in Table II. The DC motor was deployed to provide a load torque of 0.77 pu. The newly developed MPC scheme was compared against a state-of-the-art PI controller in all test cases listed in Table II.

TABLE I: Design data of the test bed.

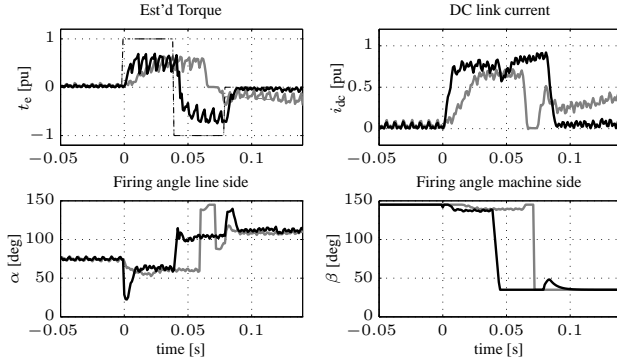| Parameter	Value	Unit
Line voltage	400	V
Line frequency	50	Hz
Rated line current	20.7	A
Rated DC current	26.6	A
Rated stator voltage	400	V
Rated stator current	21	A
Rated stator frequency	50	Hz
Rated electrical power	11.6	kW
Rated rotational speed	1500	rpm

Fig. 9: Torque step test: State-of-the-art PI controller (gray) vs. MPC (black). Torque references are indicated by the dash-dotted lines.
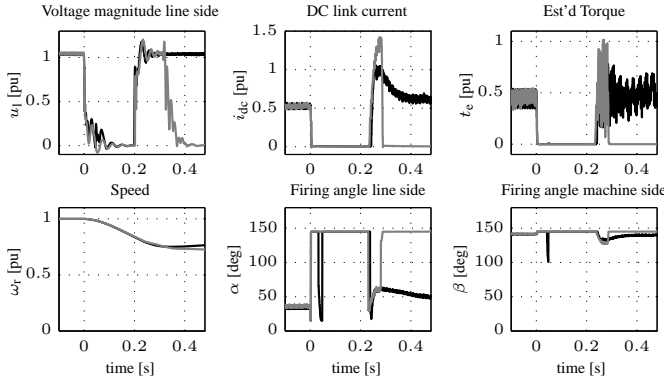

Fig. 10: Test case 8: Circuit breaker test at 1 pu speed. State-of-the-art PI controller (gray) vs. MPC (black).

Note that the presented test cases represent extreme drive situations, for which no grid standards must be observed. In the standard configuration of the LCI control system, the drive would simply trip if the grid voltage were to fall under a certain threshold. This threshold was deactivated during the run of the test cases.

The proposed MPC solution was able to handle all tested cases without tripping or major issues. Also the PI solution – though not developed for this task – was able to handle the power losses without problems in test cases 1, 2, 3, 5 and 7. Trips and speed regulation problems appeared in cases 4, 6 and 8, when a high load torque was requested. To sustain a high load torque, a high DC link current is required. At the

TABLE II: Summary of the test conditions for voltage outage tests at the test bed.

Test case No.	Opening duration [ms]	Speed [pu]	Load torque [pu]
1	40	0.5	0
2	40	0.5	0.77
3	40	1.0	0
4	40	1.0	0.77
5	200	0.5	0
6	200	0.5	0.77
7	200	1.0	0
8	200	1.0	0.77

return of the grid voltage, the controller must thus strike a subtle balance between quickly returning to a high enough current, and not overcharging the DC current. The situation is slightly worse after the longer 200 ms voltage outage, since the DC motor has more time to slow the drive down.

For the sake of brevity we present only the most challenging test conditions, which prevail during test case 8. The test results for test case 8 are shown in Figure 10. The figure shows the grid voltage magnitude computed from the measured phase-to-phase voltages, the measured DC link current, estimated torque and speed as well as the firing angles on the grid and machine side. During the voltage dip the normal thyristor firing is interrupted. In Figure 10 this can be noted as an increase of the firing angles to 145 degrees. For the MPC solution the thyristor firing is released briefly after around 40 ms, which can be seen as sudden change of the firing angles; however to no effect on the DC current. After the return of the grid voltage, firing of the firing angles is resumed and the firing angles are set to quickly increase the DC link current. Under PI control the DC current reference is limited to 1 pu. Yet the DC current overshoot is high enough to trigger an overcurrent trip and stop the drive operation. The MPC on the other hand increases the DC current to roughly 1 pu, and no trip is triggered.

C. Line and Machine AC Waveforms

Finally we provide plots showing the line side and machine side AC waveforms. The plots show actual measurements of the control system, namely a phase-to-phase voltage on the line side, a phase currents on the line side and a phase-to-phase voltage on the machine side of the converter. These measurements are shown in Figure 11, once for the PI controller and once for the proposed MPC solution. The left plot (Fig. 11a) shows the waveforms under steady-state conditions, whereas the right plot (Fig. 11b) shows the waveforms during transients, caused by a disturbance of the torque reference in form of a pulse train of reference steps with a magnitude of 0.2 pu and a pulse width of 50 ms. In both situations the machine is rotating with nominal speed, and a load torque of 0.2 pu is applied.

It can be observed that the line side commutations are much faster than the machine side commutations, reflecting the fact that the inductances on the machine side are larger than the inductances on the line side. Furthermore, in the steady-state scenario, the shown current ripple is somewhat higher with MPC compared to the PI solution, which is due to differences in the timing of the thyristor firings on the line side relative to the firings on the machine side. The waveforms under transient conditions show no significant differences between the PI controller and the MPC solution.

VII. CONCLUSION

The paper considered nonlinear model predictive control for torque regulation of a synchronous machine supplied by current source converters. In contrast to standard PI controllers, the MPC formulation does not impose a cascaded control structure, but uses both the rectifier and inverter angles
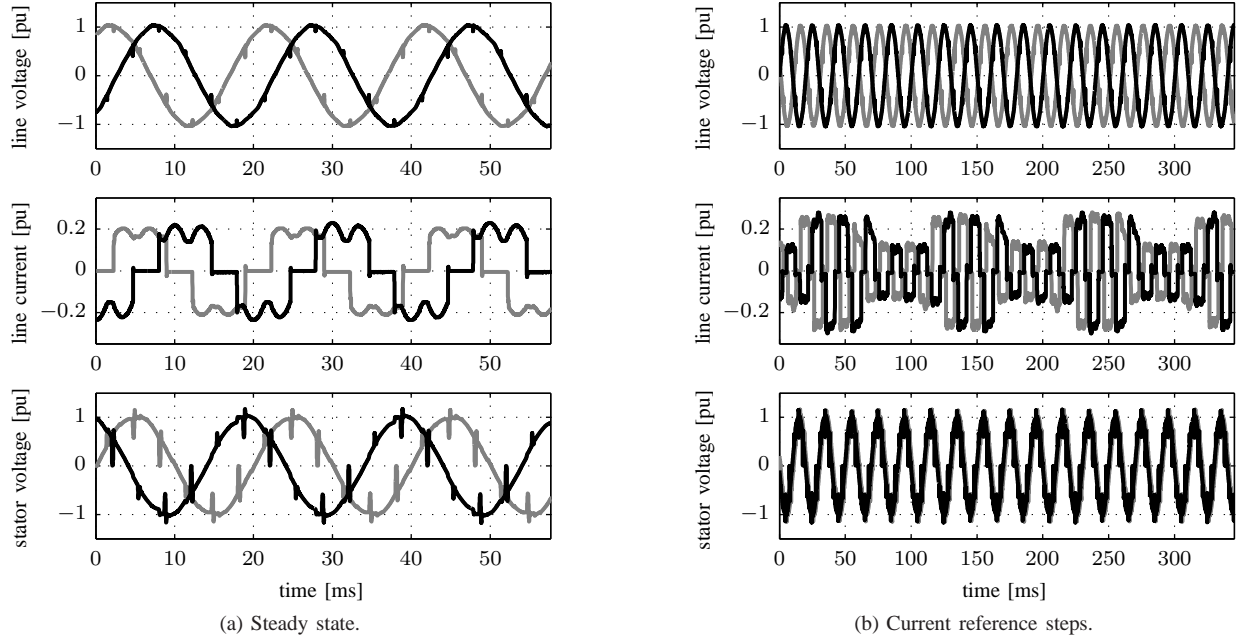
(a) Steady state.

(b) Current reference steps.

Fig. 11: Waveforms of the line voltage, the line current and the stator voltage. State-of-the-art PI controller (gray) vs. MPC (black).

simultaneously to stabilize the system state and control the torque. This increases the ability to stabilize the system and reject disturbances. Experimental verification on a 11.6 kW low voltage test bed indeed show that the controller can track the torque reference in the presence of power outages where a traditional PI controller fails. Thus, the proposed controller increases the system ability of power loss ride through. After these successful tests on a low voltage test bed, the next step will be to implement and verify the proposed controller on a medium-voltage drive.

APPENDIX

Let L_md, L_mq be the direct and quadrature axis magnetizing inductance respectively. Let $L_{\mathrm{s}\sigma}$ be the stator leakage inductance and let L_kd be the damper winding and magnetizing winding leakage inductance (Canay inductance). Let

$$\mathbf{L}_\mathrm{d} := \begin{bmatrix} L_\mathrm{sd} & L_\mathrm{md} & L_\mathrm{md} \\ L_\mathrm{md} & L_\mathrm{rd} & L_\mathrm{fd} \\ L_\mathrm{md} & L_\mathrm{fd} & L_\mathrm{f} \end{bmatrix}, \quad \mathbf{L}_\mathrm{q} := \begin{bmatrix} L_\mathrm{sq} & L_\mathrm{mq} \\ L_\mathrm{mq} & L_\mathrm{rq} \end{bmatrix},$$

where $L_\mathrm{sd} = L_\mathrm{md} + L_{\mathrm{s}\sigma}$, $L_\mathrm{rd} = L_\mathrm{md} + L_{\mathrm{s}\sigma} + L_\mathrm{kd}$, $L_\mathrm{f} = L_\mathrm{md} + L_{\mathrm{f}\sigma} + L_\mathrm{kd}$, $L_\mathrm{fd} = L_\mathrm{md} + L_\mathrm{kd}$ and $L_\mathrm{sq} = L_\mathrm{md} + L_{\mathrm{s}\sigma}$, $L_\mathrm{rq} = L_\mathrm{mq} + L_{\mathrm{s}\sigma}$. The stator and rotor currents and fluxes satisfy the flux linkage equations

$$\begin{bmatrix} \psi_\mathrm{sd} \\ \psi_\mathrm{rd} \\ \psi_\mathrm{f} \end{bmatrix} = \mathbf{L}_\mathrm{d} \begin{bmatrix} i_\mathrm{sd} \\ i_\mathrm{rd} \\ i_\mathrm{f} \end{bmatrix}, \quad \begin{bmatrix} \psi_\mathrm{sq} \\ \psi_\mathrm{rq} \end{bmatrix} = \mathbf{L}_\mathrm{q} \begin{bmatrix} i_\mathrm{sq} \\ i_\mathrm{rq} \end{bmatrix}. \quad (27)$$

The flux linkage equations (27) can be rewritten

$$\begin{bmatrix} \psi_\mathrm{sd} \\ i_\mathrm{rd} \\ i_\mathrm{f} \end{bmatrix} = \tilde{\mathbf{L}}_\mathrm{d} \begin{bmatrix} i_\mathrm{sd} \\ \psi_\mathrm{rd} \\ \psi_\mathrm{f} \end{bmatrix}, \quad \begin{bmatrix} \psi_\mathrm{sq} \\ i_\mathrm{rq} \end{bmatrix} = \tilde{\mathbf{L}}_\mathrm{q} \begin{bmatrix} i_\mathrm{sq} \\ \psi_\mathrm{rq} \end{bmatrix}. \quad (28)$$

Explicit expressions for $\tilde{\mathbf{L}}_\mathrm{d}$ and $\tilde{\mathbf{L}}_\mathrm{q}$ are omitted for brevity. Using (28) we can write the damper winding currents as a function of the stator currents and damper winding flux linkages as follows

$$\begin{bmatrix} i_\mathrm{rd} \\ i_\mathrm{rq} \end{bmatrix} = \underbrace{\begin{bmatrix} \tilde{L}_{\mathrm{d},31} & 0_{1\times 1} \\ 0_{1\times 1} & \tilde{L}_{\mathrm{q},31} \end{bmatrix}}_{\mathbf{M}_1} \begin{bmatrix} i_\mathrm{sd} \\ i_\mathrm{sq} \end{bmatrix} + \underbrace{\begin{bmatrix} \tilde{L}_{\mathrm{d},33} & 0_{1\times 1} \\ 0_{1\times 1} & \tilde{L}_{\mathrm{q},33} \end{bmatrix}}_{\mathbf{M}_2} \begin{bmatrix} \psi_\mathrm{rd} \\ \psi_\mathrm{rq} \end{bmatrix} + \underbrace{\begin{bmatrix} \tilde{L}_{\mathrm{d},23} \\ 0_{1\times 1} \end{bmatrix}}_{\mathbf{M}_3} \psi_\mathrm{f}. \quad (29)$$

Furthermore we can write the stator fluxes as a function of the stator currents and damper winding flux linkages as follows

$$\begin{bmatrix} \psi_\mathrm{sd} \\ \psi_\mathrm{sq} \end{bmatrix} = \underbrace{\begin{bmatrix} \tilde{L}_{\mathrm{d},11} & 0_{1\times 1} \\ 0_{1\times 1} & \tilde{L}_{\mathrm{q},11} \end{bmatrix}}_{\mathbf{M}_4} \begin{bmatrix} i_\mathrm{sd} \\ i_\mathrm{sq} \end{bmatrix} + \underbrace{\begin{bmatrix} \tilde{L}_{\mathrm{d},12} & 0_{1\times 1} \\ 0_{1\times 1} & \tilde{L}_{\mathrm{q},12} \end{bmatrix}}_{\mathbf{M}_5} \begin{bmatrix} \psi_\mathrm{rd} \\ \psi_\mathrm{rq} \end{bmatrix} + \underbrace{\begin{bmatrix} \tilde{L}_{\mathrm{d},13} \\ 0_{1\times 1} \end{bmatrix}}_{\mathbf{M}_6} \psi_\mathrm{f}. \quad (30)$$

REFERENCES

[1] A. B. Plunkett and F. G. Turnbull, "Load Commutated Inverter Synchronous Motor Drive Without a Shaft Position Sensor," *Industrial Applications, IEEE Transactions on*, vol. IA-15, pp. 63 – 71, 1979.

[2] A. Tessarolo, C. Bassi, G. Ferrari, D. Giulivo, R. Macuglia, and R. Menis, "Investigation Into the High-Frequency Limits and Performance of Load Commutated Inverters for High-Speed Synchronous Motor Drives," *Industrial Electronics, IEEE Transactions on*, vol. 60, no. 6, pp. 2147–2157, June 2013.

[3] S. Mohamadian, M. Khanzade, S. Castellan, and A. Tessarolo, "LCI-fed Wound-Field Synchronous Motors: A Technology Status Review and New Development Trends," in *AEIT Annual Conference - From Research to Industry: The Need for a More Effective Technology Transfer (AEIT)*, Sept 2014, pp. 1–6.

[4] S. Singh and B. Singh, "Power Quality Improvement Using Optimized Passive Filter for 12-Pulse Rectifier-Chopper in LCI fed Synchronous Motor Drives," in *Information and Communication Technologies (WICT), 2011 World Congress on*, Dec 2011, pp. 1104–1111.

[5] E. Wiechmann, P. Aqueveque, R. Burgos, and J. Rodriguez, "On the Efficiency of Voltage Source and Current Source Inverters for High-Power Drives," *Industrial Electronics, IEEE Transactions on*, vol. 55, pp. 1771 – 1782, April 2008.

[6] R. Bhatia, H. Krattiger, A. Bonanini, D. Schafer, J. Inge, and G. Sydnor, "Adjustable speed drive with a single 100-MW synchronous motor," *ABB Review*, vol. 6, pp. 14 –20, 1998.

[7] T. Wymann and P. Jörg, "Power loss ride-through in a variable speed drive system," in *Petroleum and Chemical Industry Conference (PCIC) Europe*, June 2014, pp. 1–9.

[8] P. Jörg, A. Tresch, and M. Bruha, "A model based approach to optimize controls of a large LCI VSD for minimal grid-side sub-synchronous torsional interaction," in *Petroleum and Chemical Industry Conference (PCIC) Europe*, May 2013, pp. 1–7.

[9] A. Jain and V. Ranganathan, "Improved control of load commuted inverter fed salient pole wound field synchronous motor using field oriented technique," in *Energy Conversion Congress and Exposition (ECCE)*, Sept 2012, pp. 1238–1245.

[10] F. Morel, J.-M. Retif, X. Lin-Shi, and C. Valentin, "Permanent Magnet Synchronous Machine Hybrid Torque Control," *Industrial Electronics, IEEE Transactions on*, vol. 55, no. 2, pp. 501–511, 2008.

[11] T. Geyer, G. Papafotiou, and M. Morari, "Model Predictive Direct Torque Control - Part I: Concept, Algorithm, and Analysis," *Industrial Electronics, IEEE Transactions on*, vol. 56, no. 6, pp. 1894–1905, June 2009.

[12] P. Cortes, M. Kazmierkowski, R. Kennel, D. Quevedo, and J. Rodriguez, "Predictive control in power electronics and drives," *Industrial Electronics, IEEE Transactions on*, vol. 55, no. 12, pp. 4312–4324, 2008.

[13] S. Bolognani, S. Bolognani, L. Peretti, and M. Zigliotto, "Design and Implementation of Model Predictive Control for Electrical Motor Drives," *Industrial Electronics, IEEE Transactions on*, vol. 56, no. 6, pp. 1925–1936, June 2009.

[14] S. Almér, S. Mariéthoz, and M. Morari, "Sampled Data Model Predictive Control of a Voltage Source Inverter for Reduced Harmonic Distortion," *Control Systems Technology, IEEE Transactions on*, vol. 21, no. 5, pp. 1907–1915, Sept 2013.

[15] S. Almér, S. Mariéthoz, and M. Morari, "Dynamic Phasor Model Predictive Control of Switched Mode Power Converters," *Control Systems Technology, IEEE Transactions on*, vol. 23, no. 1, pp. 349–356, Jan 2015.

[16] S. Richter, S. Mariéthoz, and M. Morari, "High-Speed Online MPC Based on a Fast Gradient Method Applied to Power Converter Control," in *American Control Conference (ACC)*, 2010, pp. 4737–4743.

[17] Y. Xie, R. Ghaemi, J. Sun, and J. Freudenberg, "Model Predictive Control for a Full Bridge DC/DC Converter," *Control Systems Technology, IEEE Transactions on*, vol. 20, no. 1, pp. 164–172, Jan 2012.

[18] S. Mariéthoz, A. Domahidi, and M. Morari, "High-Bandwidth Explicit Model Predictive Control of Electrical Drives," *Industry Applications, IEEE Transactions on*, vol. 48, no. 6, pp. 1980–1992, Nov 2012.

[19] B. Houska, H. Ferreau, and M. Diehl, "An Auto-Generated Real-Time Iteration Algorithm for Nonlinear MPC in the Microsecond Range," *Automatica*, vol. 47, no. 10, pp. 2279–2285, 2011.

[20] S. Almér, T. Besselmann, and J. Ferreau, "Nonlinear Model Predictive Torque Control of a Load Commutated Inverter and Synchronous Machine," in *International Power Electronics Conference (IPEC - ECCE-ASIA)*, May 2014, pp. 3563–3567.

[21] R. H. Park, "Two Reaction Theory of Synchronous Machines generalized Method of Analysis-Part I," *AIEE Transactions*, vol. 48, pp. 716 – 727, 1929.

[22] D. Schröder, *Elektrische Antriebe - Regelung von Antriebssystemen*, 3rd ed. Berlin; Heidelberg: Springer Verlag, 2009.

[23] BBC AG, *Silizium Stromrichter Handbuch*. Baden, Mannheim: BBC, 1971.

[24] R. S. Colby, T. A. Lipo, and D. W. Novotny, "A State Space Analysis of LCI Fed Synchronous Motor Drives in the Steady State," *Industry Applications, IEEE Transactions on*, vol. IA-21, no. 4, pp. 1016–1022, July 1985.

[25] H. Burzanowska, "Dual-three phase synchronous motor model," ABB Switzerland Ltd, Tech. Rep., 2004.

[26] W. Leonhard, *Control of Electrical Drives*. Berlin; Heidelberg; New York: Springer-Verlag, 2001.

[27] H. J. Ferreau, H. G. Bock, and M. Diehl, "An online active set strategy to overcome the limitations of explicit MPC," *International Journal of Robust and Nonlinear Control*, vol. 18, no. 8, pp. 816–830, 2008.

[28] H. Peyrl, A. Zanarini, T. Besselmann, J. Liu, and M.-A. Boéchat, "Parallel implementations of the fast gradient method for high-speed MPC," *Control Engineering Practice*, vol. 33, pp. 22 – 34, 2014.

[29] J. Nocedal and S. Wright, *Numerical Optimization*, 2nd ed., ser. Springer Series in Operations Research and Financial Engineering. Springer, 2006.

[30] M. Diehl, H. Bock, J. Schlöder, R. Findeisen, Z. Nagy, and F. Allgöwer, "Real-time optimization and nonlinear model predictive control of processes governed by differential-algebraic equations," *Journal of Process Control*, vol. 12, no. 4, pp. 577–585, 2002.

[31] H. Ferreau, C. Kirches, A. Potschka, H. Bock, and M. Diehl, "qpOASES: A parametric active-set algorithm for quadratic programming," *Mathematical Programming Computation*, vol. 6, no. 4, pp. 327–363, 2014.

[32] B. Anderson and J. Moore, *Optimal Filtering*. Prentice-Hall, Englewood Cliffs, N.J, 1979.

Thomas J. Besselmann received his B.Sc. degree in general engineering science in 2003 and his Dipl.-Ing. degree in mechatronics in 2005 from Hamburg University of Technology, Germany. In 2010 he obtained his Ph.D. degree in electrical engineering at the Automatic Control Laboratory, ETH Zurich, Switzerland. Currently he is employed as senior scientist in the Control & Optimization group at ABB Corporate Research, Switzerland. His research interests include high-speed control methods for constrained systems, in particular model predictive control, and their application to automotive and power electronics systems.

Stefan Almér was born in Stockholm, Sweden. He received the M.Sc. degree in Engineering Physics in 2003 and the Ph.D. degree in Optimization and Systems Theory in 2008, both from the Royal Institute of Technology (KTH), Stockholm. Between 2008 and 2012 he held a research position at the Automatic Control Laboratory, ETH Zürich, Switzerland. Currently he is employed as senior scientist in the Control & Optimization group at ABB Corporate Research, Switzerland. His research interests include switched systems, model predictive control and control of power electronics.

Hans Joachim Ferreau studied mathematics and computer science at Heidelberg University, Germany, where he received a master degree in 2007. In 2011 he obtained a PhD degree in Electrical Engineering from KU Leuven, Belgium, with a doctoral thesis on numerical methods for fast model predictive control. In 2012 he joined ABB's corporate research center in Baden-Dättwil, Switzerland, where he currently works as senior scientist on various applications of optimization-based control. His current research is focussing on tools and algorithms for embedded optimization, such as model predictive control.